POLITECNICO DI TORINO
Repository ISTITUZIONALE

Hybrid WaveletDeep Learning Framework for Fluorescence Microscopy Images Enhancement

(Article begins on next page)

19 November 2024

RESEARCH ARTICLE OPEN ACCESS

Hybrid Wavelet-Deep Learning Framework for Fluorescence Microscopy Images Enhancement

Francesco Branciforti[1] | Maura Maggiore[1] | Kristen M. Meiburger[1] | Tania Pannellini[2] | Massimo Salvi[1]

[1]Biolab, PoliToBIOMed Lab, Department of Electronics and Telecommunications, Politecnico di Torino, Turin, Italy | [2]Division of Hematopathology, IEO European Institute of Oncology IRCCS, Milan, Italy

Correspondence: Francesco Branciforti (francesco.branciforti@polito.it)

ABSTRACT

Fluorescence microscopy is a powerful tool for visualizing cellular structures, but it faces challenges such as noise, low contrast, and autofluorescence that can hinder accurate image analysis. To address these limitations, we propose a novel hybrid image enhancement method that combines wavelet-based denoising, linear contrast enhancement, and convolutional neural network-based autofluorescence correction. Our automated method employs Haar wavelet transform for noise reduction and a series of adaptive linear transformations for pixel value adjustment, effectively enhancing image quality while preserving crucial details. Furthermore, we introduce a semantic segmentation approach using CNNs to identify and correct autofluorescence in cellular aggregates, enabling targeted mitigation of unwanted background signals. We validate our method using quantitative metrics, such as signal-to-noise ratio (SNR) and peak signal-to-noise ratio (PSNR), demonstrating superior performance compared to both mathematical and deep learning-based techniques. Our method achieves an average SNR improvement of 8.5 dB and a PSNR increase of 4.2 dB compared with the original images, outperforming state-of-the-art methods such as BM3D and CLAHE. Extensive testing on diverse datasets, including publicly available human-derived cardiosphere and fluorescence microscopy images of bovine endothelial cells stained for mitochondria and actin filaments, showcases the flexibility and robustness of our approach across various acquisition conditions and artifacts. The proposed method significantly improves fluorescence microscopy image quality, facilitating more accurate and reliable analysis of cellular structures and processes, with potential applications in biomedical research and clinical diagnostics.

1 | Background

Fluorescence microscopy is a widely utilized technique in medical optical imaging that enables the analysis of molecular structures within biological samples and the visualization of cellular processes at the microscopic level [1]. This technique employs fluorophores, fluorescent substances used to label the sample. Fluorophores are excited upon absorbing light from a source, and as they return to their ground state, they emit fluorescent light at a longer wavelength, allowing for the imaging of fluorescent components within the sample [2].

Despite its widespread use, fluorescence microscopy exhibits practical limitations that can introduce artifacts and challenges during the image acquisition process [3]. These limitations primarily impact crucial aspects such as resolution [4], contrast [5], signal-to-noise ratio [6], and overall image quality [7]. Several factors contribute to these challenges, including improper sample illumination, particularly in cases where thick cellular aggregates are present, resulting in blurred objects in the acquired images. Additionally, the loss of fluorescence intensity from the fluorophores used to label specific biological structures of interest and the emission of intrinsic fluorescent light from

surrounding biological structures not of interest can interfere with the clear and accurate visualization of the objects under examination [8]. This intrinsic emission, commonly referred to as autofluorescence, arises when inherent components within the biological sample emit light upon excitation, even in the absence of external fluorophores. Such autofluorescence complicates image analysis, as it introduces unwanted background signals that can challenge the differentiation between the intended fluorescence from the applied fluorophores and the sample's natural fluorescence. Especially when these emissions overlap with the fluorescence of interest, the clarity and specificity of the image can be significantly degraded [9].

To overcome these constrains and improve the quality of fluorescence microscopy images, various techniques and strategies have been developed. These include advancements in imaging hardware, such as optimizing the illumination system and selecting appropriate filters and light sources [10]. However, these approaches often require significant time and expertise from the user, as specific parameter settings must be determined for each acquisition based on the biological structures under examination. Moreover, controlling multiple critical aspects simultaneously may not be feasible [11].

In recent years, digital image processing has seen the development of several techniques aimed at reducing artifacts in fluorescence images, thereby enhancing subsequent quantitative analysis performed by operators or artificial intelligence algorithms. Two examples of such techniques are block-matching and 3D filtering (BM3D) [12] and contrast-limited adaptive histogram equalization (CLAHE) [13]. BM3D is an advanced image denoising technique that identifies similar blocks in noisy images, stacks them into 3D groups, and applies collaborative filtering in the transform domain, leveraging local redundancies to efficiently reduce noise while retaining image details. On the other hand, CLAHE is an adaptive image enhancement technique that focuses on improving local contrast and enhancing details in various types of images, including fluorescence microscopy data. Unlike traditional histogram equalization, CLAHE divides the image into smaller regions called tiles and limits the contrast enhancement within each tile to prevent excessive amplification of noise or artifacts. This adaptive approach enables CLAHE to handle images with varying local contrast and produce high-quality visual results. Both BM3D and CLAHE have been widely employed as processing steps in quantitative analysis pipelines across various imaging domains, including but not limited to fluorescence microscopy [14–16]. While these techniques offer generality, one major drawback is the need for parameter tuning, as each image may require a different subset of parameters [17]. Consequently, when applied to large datasets with fixed parameters, the results obtained often fall short of optimal noise reduction and image quality improvement for individual images.

To improve quality in fluorescence microscopy images, it is crucial to develop a robust and widely applicable strategy. This strategy should encompass various aspects, including increasing the signal-to-noise ratio, enhancing object visibility and contrast during image acquisition, as well as effectively correcting luminous artifacts, such as autofluorescence. Current methods offer a limited ability to handle diverse datasets, or they often fail to address all these challenges simultaneously. Therefore, there is a need for an automated, versatile approach that can enhance fluorescence microscopy images across different experimental conditions and biological samples, while preserving structural information.

This study aims to develop an AI-based framework that effectively overcomes the current constrains in fluorescence microscopy using computer vision techniques. The proposed framework specifically targets key issues such as noise reduction, contrast enhancement, and artifact correction in fluorescence microscopy images. The main contributions of this paper can be summarized as follows:

- A novel method for denoising and enhancing high-resolution fluorescence images using a combination of Haar wavelet transform for frequency analysis and linear mathematical transformations for pixel value adjustment. This approach effectively reduces noise, enhances contrast, and significantly improves image clarity and detail.

- An innovative approach for correcting autofluorescence in cellular aggregates using a convolutional neural network (CNN) for semantic segmentation. By leveraging the semantic content identified by the CNN, our method enables targeted correction of autofluorescence, enhancing the visibility and accuracy of the desired fluorescent structures.

- Rigorous validation using quantitative metrics such as signal-to-noise ratio (SNR) and peak signal-to-noise ratio (PSNR), with comparison to state-of-the-art methods including BM3D, CLAHE, and deep learning-based approaches. Our evaluations demonstrate the superior performance and effectiveness of the proposed approach.

- Extensive testing on diverse datasets, including two publicly available datasets: one containing human-derived cardiospheres, and another featuring actin filaments and mitochondria in bovine pulmonary artery endothelial cells. These datasets encompass various acquisition conditions, including different SNR levels, magnifications, demonstrating the versatility of our approach across different cellular structures and imaging parameters.

This paper is structured as follows: Section 2 provides a comprehensive overview of the proposed method, whereas Section 3 details the experimental results. Finally, Sections 4 and 5 offer a thorough discussion of the overall work.

2 | Methods

An overview of the entire methodology is illustrated in Figure 1. The presented method aims to enhance fluorescence microscopy images by taking three specific actions to address the challenges of this imaging modality:

- Enhancement: a linear mathematical transformation is applied to improve image quality by enhancing the contrast and visibility of objects, ensuring the preservation of image morphology.
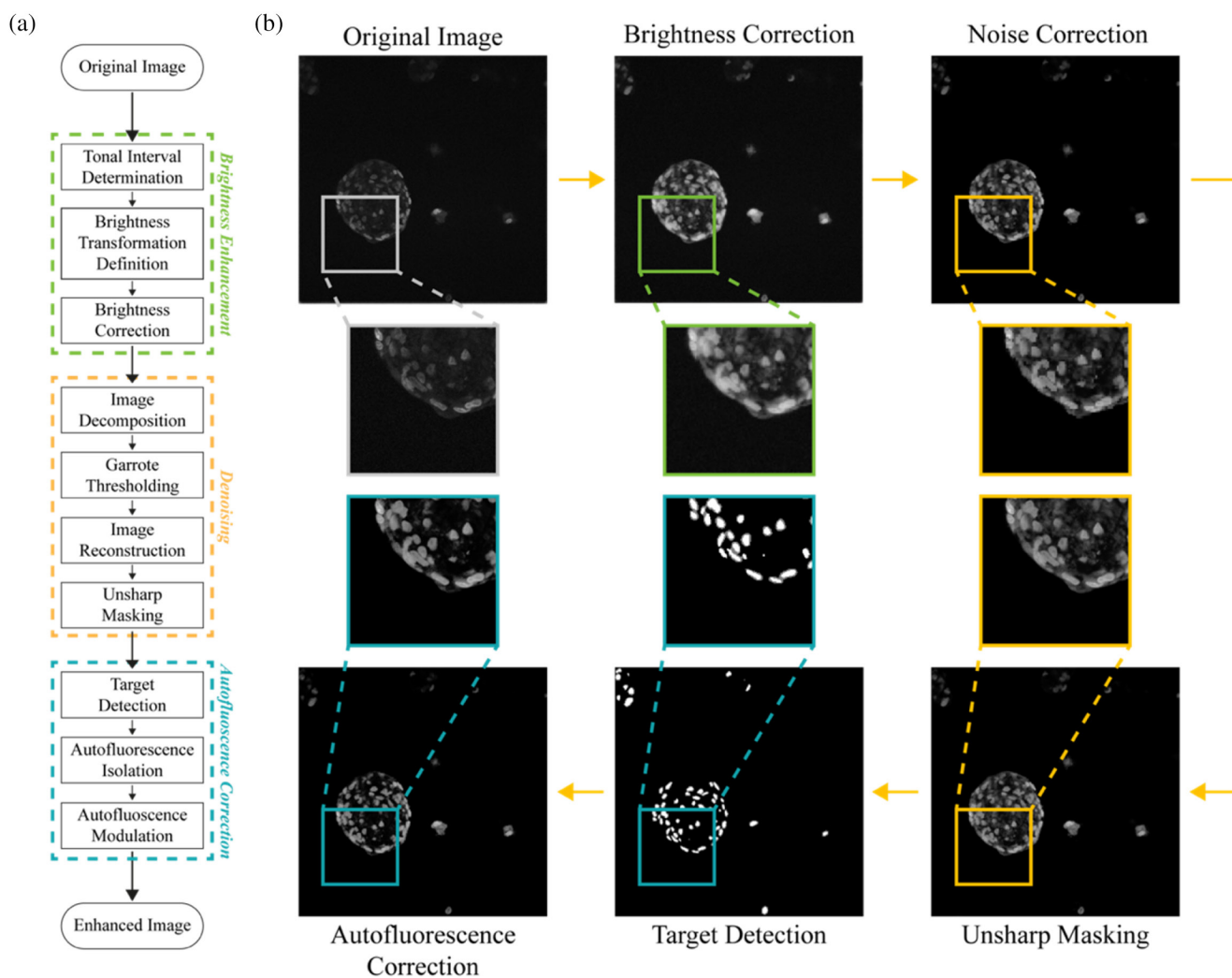
FIGURE 1 | Comprehensive illustration of the proposed methodology. (a) A schematic flowchart delineating each procedural step of the methodology. (b) A step-by-step visual depiction of the successive effects of each processing step on the image.

TABLE 1 | Overview of the datasets employed in our research, detailing the source, number of images, image dimensions, primary cellular content, and the magnification level.

Dataset	Type of acquisition	Number of slices/images	Image dimension on XY plane (pixels)	Content	Magnification
Hagen et al. [18]	2D	400	2048×2048	Actin and mitochondria	20×, 60×
Cardiosphere [19]	3D	1160	1024×1024	Membrane and cell nuclei	40×

- Denoising: through frequency analysis methods, the approach targets background noise by precisely identifying and removing high-frequency components. This results in an elevated SNR while maintaining semantic content.

- Correction of luminous artifacts: to mitigate the effects of light interference from autofluorescence emitted by surrounding biological structures, a deep neural network is employed. This generates a segmentation mask that precisely identifies the target structures. By leveraging this mask, the method focuses its correction efforts specifically on the

intended fluorescence, differentiating it from unintended emissions from nontargeted cell structures, and thus enhancing the visibility of the desired objects.

2.1 | Dataset

In this study, we utilized two distinct datasets to evaluate our proposed methods (Table 1). The first dataset consists of fluorescence microscopy images of actin filaments and

mitochondria in bovine pulmonary artery endothelial cells, extracted from the GigaScience Database, and originally obtained from the work of Hagen et al. [18]. Actin filaments were visualized using AlexaFluor 488 phalloidin, a direct fluorescent stain that binds to F-actin, while mitochondria were labeled with MitoTracker Red CMXRos, a cell-permeant probe that accumulates in active mitochondria. For each cellular structure, two versions are available: one with low SNR and one with high SNR. These different SNR levels were obtained by adjusting the acquisition time: high exposure (actin) 500 ms; low exposure (actin) 20 ms; high exposure (mitochondria) 400 ms; low exposure (mitochondria) 15 ms. The dataset comprises 400 images, divided based on the Numerical Aperture used for acquisition (20× and 60×), and includes actin and mitochondria images for both SNR levels. The actin images were captured in the green channel (excitation: 495 nm, emission: 519 nm), whereas mitochondria were imaged in the red channel (excitation: 579 nm, emission: 599 nm). The images were saved with a size of 2048 × 2048 pixels, with a scan resolution of 325 nm.

The second dataset comprises human-derived cardiospheres, which mimic stem cell systems, obtained from a publicly available dataset [19]. Cardiospheres are three-dimensional aggregates of cardiac progenitor cells that represent a vitro model of the cardiac stem cell niche. This dataset comprises 27 cardiospheres caputerd across 1160 slides. The imaging was conducted using two separate fluorescent channels. The cellular membranes were imaged in the red channel (excitation: 557 nm, emission: 576 nm) using TRITC-labeled phalloidin, while cell nuclei were captured in the blue channel (excitation: 358 nm, emission: 461 nm) using DAPI staining. Each image slice has a resolution of 1024 × 1024 pixels, with a voxel size of $0.345 \times 0.345 \times 0.432 \, \mu m/pixel^3$, providing highly detailed views of these complex cellular structures.

It is important to note that while the original images in our datasets are color-coded, all image processing steps are performed on grayscale versions of these images. This method enables more consistent and effective processing across many fluorescence channels.

2.2 | Brightness Enhancement Function

In fluorescence microscopy, one common challenge is nonuniform illumination, which results in some structures appearing darker or more obscured than others. To address this issue, we developed an enhancement algorithm designed to increase the brightness of darker regions without distorting well-lit areas, primarily through utilizing ascending linear functions to amplify pixel intensity values. Before starting the enhancement procedure, a preprocessing step is carried out where we applied min–max normalization to convert the original 16-bit acquisitions to 8-bit images. This allows us to work with pixel values ranging from 0 to 255 for all images.

After this normalization, we undertake two crucial preparatory steps: Tonal Interval Determination and Slope Definition. These steps are critical in customizing the brightness enhancement function to each individual image:

1. Tonal Intervals Determination: initially, pixel values are divided into three primary tonal intervals to differentially process dark, intermediate, and light tones of the image. The division occurs dynamically, customized to each image based on its average brightness (μ_B), using the following thresholds:

$$T_{\text{dark}} = \mu_B + \frac{(255 - \mu_B)}{f_1} \quad (1)$$

$$T_{\text{mid}} = \mu_B + \frac{(255 - \mu_B)}{f_2} \quad (2)$$

where T_{dark} is the upper boundary of the dark tones' interval and T_{mid} is the upper limit of the intermediate tones. The scaling factors f_1 and f_2 are user-defined parameters that influence the calculation of these thresholds, allowing for customization in the enhancement process. In our implementation, we set $f_1 = 6$ and $f_2 = 4$, as these values were found to provide a good balance between enhancing faint objects and preserving the overall tonal distribution of the image. These values were determined through empirical testing on a representative subset of the data, considering both visual assessment and quantitative metrics such as contrast improvement and detail preservation. The choice of $f_1 > f_2$ ensures that the upper threshold (T_{mid}) is further from the median intensity compared to the lower threshold (T_{dark}), effectively capturing a wider range of tonal values for enhancement while avoiding over-amplification of noise or background regions.

Equations (1) and (2) dynamically determine tonal intervals based on each image's average brightness (μ_B), allowing our method to adapt to the wide variability in overall brightness and contrast levels often seen in fluorescence microscopy. To further increase brightness of darker objects and emphasize their contrast, we subdivided the dark interval into three subranges using two additional thresholds:

$$T_{\text{dark-low}} = \mu_B + \frac{(T_{\text{dark}} - \mu_B)}{f_{11}} \quad (3)$$

$$T_{\text{dark-mid}} = \mu_B + \frac{(T_{\text{dark}} - \mu_B)}{f_{12}} \quad (4)$$

where $T_{\text{dark-low}}$ separates the darkest tones from the mid-level dark tones, and $T_{\text{dark-mid}}$ separates the mid-level dark tones from the lighter dark tones. The scaling factors f_{11} and f_{12}, which are values less than 1 set by the user, allow to fine-tune this correction.

The optimal selection of the scaling factors was achieved through ad-hoc experiments that were based on analyzing the effect of their modifications on brightness enhancement. Specifically, the scaling factors f_1 and f_2 were determined to create intervals that enhance the pixel values within heavily shadowed objects more significantly than those within intermediate and light tones. Similarly, f_{11} and f_{12} were carefully chosen to discern background pixels, which require no

brightness adjustment, from those needing an effective increase to maintain contrast. The optimal parameters for each dataset are detailed in Table 2.

Overall, this step divides the original image dynamics into five ranges—the first three belonging to the dark tone interval, and the other two covering intermediate and light tones. A graphical representation of these divisions can be seen in Figure 2a.

2. Brightness Transformation Definition: following the identification of tonal intervals, we delineated linear brightness transformations within each range. These functions map the pixels of the original image onto an output image, which is characterized by a more balanced distribution of brightness. Each tonal range is characterized by a linear ascending function that passes through two points, defined by the combination of the initial tone thresholds (T), as x-coordinates, and the enhanced tone thresholds (T'), as y-coordinate. The transformations are defined as follows:

$$y = \begin{cases} \alpha x & 0 \leq x \leq T_{\text{dark−low}} \\ \beta\left(x - T_{\text{dark−low}}\right) + T'_{\text{dark−low}} & T_{\text{dark−low}} < x \leq T_{\text{dark−mid}} \\ \gamma\left(x - T_{\text{dark−mid}}\right) + T'_{\text{dark−mid}} & T_{\text{dark−mid}} < x \leq T_{\text{dark}} \\ \delta\left(x - T_{\text{dark}}\right) + T'_{\text{dark}} & T_{\text{dark}} < x \leq T_{\text{mid}} \\ \epsilon\left(x - T_{\text{mid}}\right) + T'_{\text{mid}} & T_{\text{mid}} < x \leq 255 \end{cases}$$

$$(5)$$

with β, γ, δ, and ϵ the slope coefficients, defined as:

$$\alpha = \frac{T'_{\text{dark−low}}}{T_{\text{dark−low}}}$$

$$\beta = \frac{\left(T'_{\text{dark−mid}} - T'_{\text{dark−low}}\right)}{\left(T_{\text{dark−mid}} - T_{\text{dark−low}}\right)}$$

$$\gamma = \frac{\left(T'_{\text{dark}} - T'_{\text{dark−mid}}\right)}{\left(T_{\text{dark}} - T_{\text{dark−mid}}\right)}$$

$$\delta = \frac{\left(T'_{\text{mid}} - T'_{\text{dark}}\right)}{\left(T_{\text{mid}} - T_{\text{dark}}\right)}$$

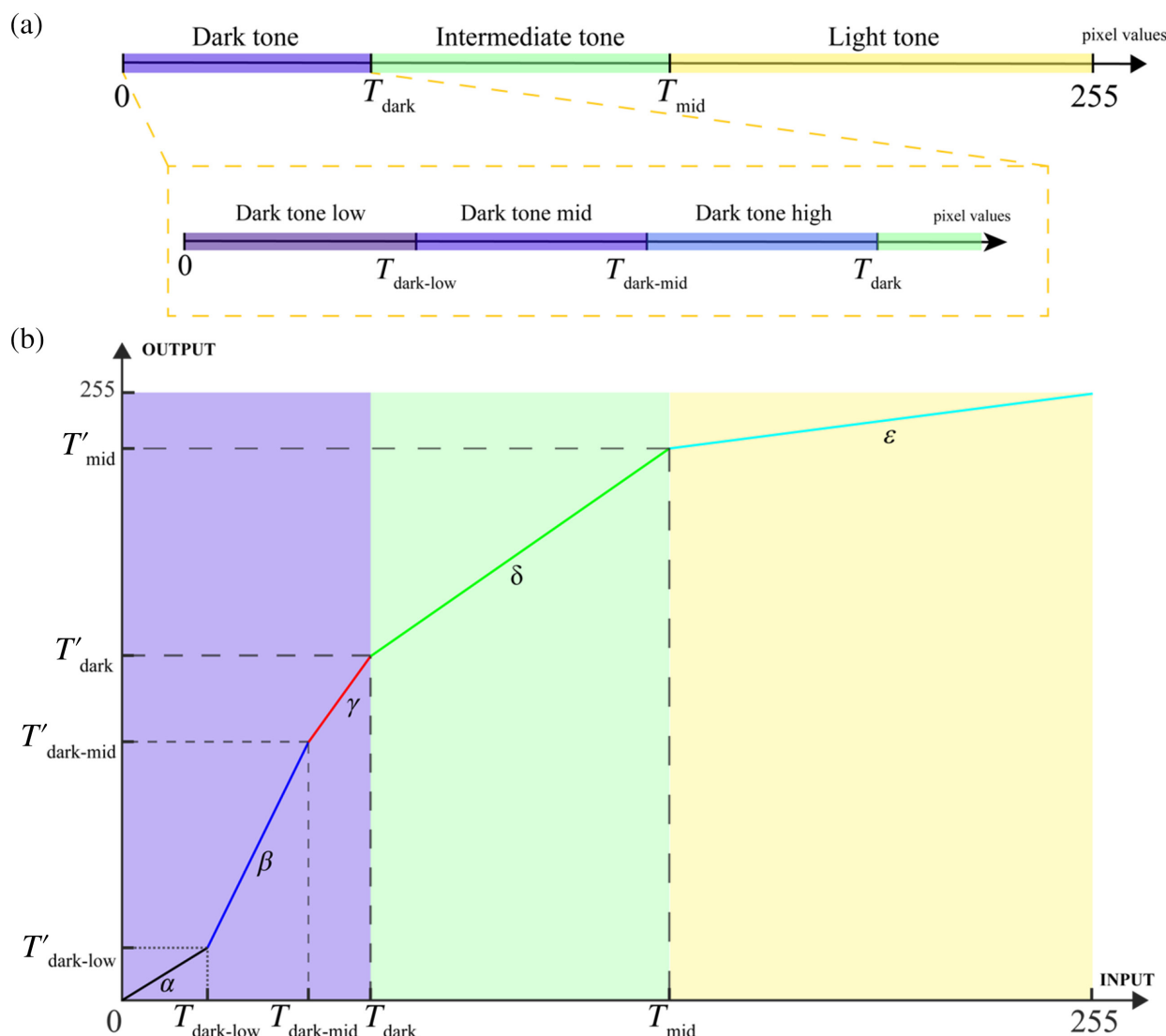$$\epsilon = \frac{\left(255 - T'_{\text{mid}}\right)}{\left(255 - T_{\text{mid}}\right)} \tag{6}$$

The terms $T'_{\text{dark−mid}}$, T'_{dark}, and T'_{mid} represent the enhanced tone thresholds, and are defined as:

$$T'_{\text{dark−mid}} = T_{\text{dark−mid}} + \text{offset}_{\text{dark−mid}}$$

$$T'_{\text{dark}} = T_{\text{dark}} + \text{offset}_{\text{dark}}$$

$$T'_{\text{mid}} = T_{\text{mid}} + \text{offset}_{\text{mid}} \tag{7}$$

With $\text{offset}_{\text{dark−mid}}$, $\text{offset}_{\text{dark}}$, and $\text{offset}_{\text{mid}}$ user-defined parameters. These parameters control the boundaries between the

TABLE 2 | Comprehensive overview of the best-performing hyperparameters identified for each dataset during the tuning process.

| Parameter	Description	Range	Best values for the dataset				
			Actin 20×	Actin 60×	Mitochondria 20×	Mitochondria 60×	Cardiosphere
$\text{offset}_{\text{dark−mid}}$	Offset between dark and mid tones	(50–100)	60	60	80	100	90
$\text{offset}_{\text{dark}}$	Offset for dark tones	(60–120)	70	70	90	110	100
$\text{offset}_{\text{mid}}$	Offset for mid tones	(80–150)	100	100	120	140	130
D	Denoising factor	(1.3–1.5)	1.32	1.32	1.37	1.32	1.42
η	Sharpening factor	(0.1, 0.2)	0.1	0.1	0.1	0.1	0.2

FIGURE 2 | Tonal interval determination and brightness transformation function definition in Image Enhancement step. (a) Pixel values are divided into five tonal ranges to enhance both dark and light regions within the image. This segmentation is based on dynamically calculated thresholds influenced by the image's average brightness and user-defined scaling factors. (b) Definition of linear transformations, designed to map pixel values from the original to the output image, facilitating a balanced brightness distribution.

dark and middle tonal regions, defining the range of pixel values in each interval. The optimal configuration of these offset values is crucial for boosting the visibility of faint structures and low-intensity details while maintaining overall contrast and achieving a balanced brightness distribution. The offset values directly impact the slope coefficients (α, β, and γ), which govern the degree of pixel value expansion within each tonal interval. These coefficients provide a gradual and adaptive enhancement, with the degree of expansion decreasing from the dark to the middle interval. This ensures that the darkest regions, containing the faintest details, receive the strongest enhancement, while the middle tones are adjusted moderately to maintain natural contrast and avoid over-amplification of noise. The optimal offset values for each dataset were determined through a hyperparameter tuning process (Section 3.1), involving systematic exploration of parameter combinations guided by quantitative metrics and visual assessment. Figure 2b graphically illustrates the brightness transformation functions.

After calibrating the transformations, they are applied directly to the image to improve its brightness and contrast details. The parameters offset$_{\text{dark−mid}}$, offset$_{\text{dark}}$, and offset$_{\text{mid}}$ play a crucial role in determining the extent and distribution of brightness and contrast enhancements across the image. To illustrate their effects, Figure 3 presents a comparison of images processed with different values for these key parameters.

2.3 | Image Denoising

Fluorescence microscopy images often have noisy backgrounds with pixel intensities that resemble signal areas, making it challenging to distinguish noise from true information using conventional filters. We found Haar wavelet transform effective for this denoising task [20, 21]. The multi-scale decomposition of the Harr wavelet transform allows for the separation of noise from relevant image features at different levels of detail, making it possible to selectively remove noise without compromising the
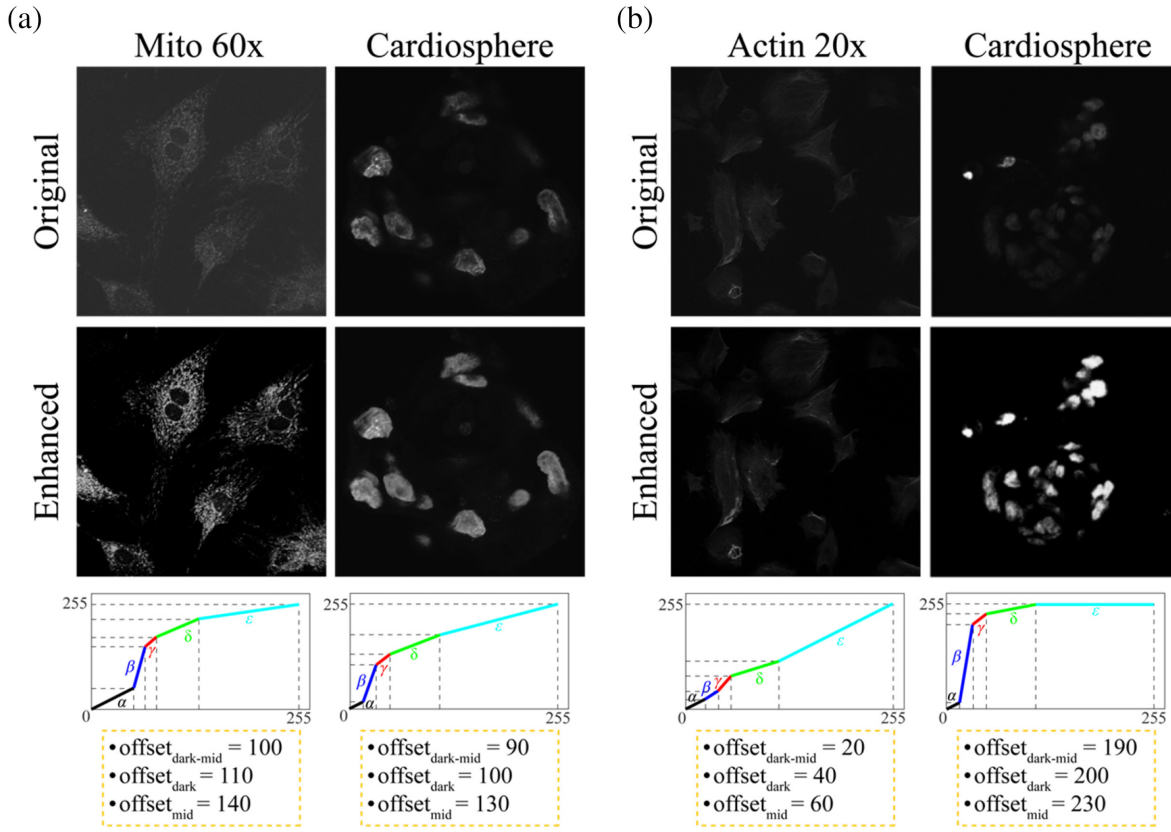
FIGURE 3 | Impact of parameters offset$_{dark-mid}$, offset$_{dark}$, and offset$_{mid}$ in the image enhancement process. (a) Examples of properly enhanced images from the ActinMito subset and the cardiosphere subset. (b) Examples from the ActinMito subset and the cardiosphere dataset showing under-enhanced and over-enhanced images, demonstrating how parameter variations affect the enhancement step.

integrity of the signal. The entire Image Denoising step is shown in Figure 4 and consists of three key steps:

1. Decomposition: the original image is decomposed with the Haar wavelet transform into four sub-images (low-low, low-high, high-low, and high-high), through convolutions with four specific kernels [21]. The LL sub-image approximates of the original image I while the LH, HL, and HH components contain information extracted from various orientations within the original image.

2. Thresholding: using Garrote Thresholding [22], each sub-image is processed to significantly minimize the noise components. The resulting sub-image is calculated as:

$$G(x, \lambda) = \begin{cases} x - \dfrac{\lambda^2}{x} & x > |\lambda| \\ 0 & x \leq |\lambda| \end{cases} \qquad (8)$$

With x the pixel value of the original sub-image and λ a threshold defined as:

$$\lambda = \begin{cases} D \times \min(\text{LL}) & \min(\text{LL}) \neq 0 \\ D \times \overline{\text{LL}} & \text{otherwise} \end{cases} \qquad (9)$$

$\overline{\text{LL}}$ denotes the updated approximation coefficients from subsequent levels of wavelet decomposition, representing further refined low-frequency components of the image. D, the Denoise

Factor, is a user-defined parameter that modulates the denoising effect in our algorithm, allowing for a flexible and adaptive approach to noise reduction. It controls the strength of the denoising process, with higher values resulting in more aggressive noise reduction and lower values preserving more of the original image detail. By tuning D for each dataset, we can strike an optimal balance between noise suppression and detail preservation, ensuring that the enhanced images maintain a high signal-to-noise ratio while retaining important structural information. The optimal D values for each dataset were determined through a hyperparameter tuning process (Section 3.1).

3. Reconstruction: finally, the resulting sub-images are reassembled through the inverse wavelet transform, which combines up-sampling and reconstruction operations.

2.4 | Unsharp Masking for Sharpness Enhancement

Wavelet denoising, while effective in reducing noise, may sometimes result in an unwanted side effect of reduced image sharpness. To mitigate this potential loss of sharpness and enhance the clarity of image details, we applied unsharp masking sharpening [23]. This sharpening method works by emphasizing the high-frequency components of the image, effectively increasing the contrast along edges and fine structures. The unsharp masking process is governed by the following equation:
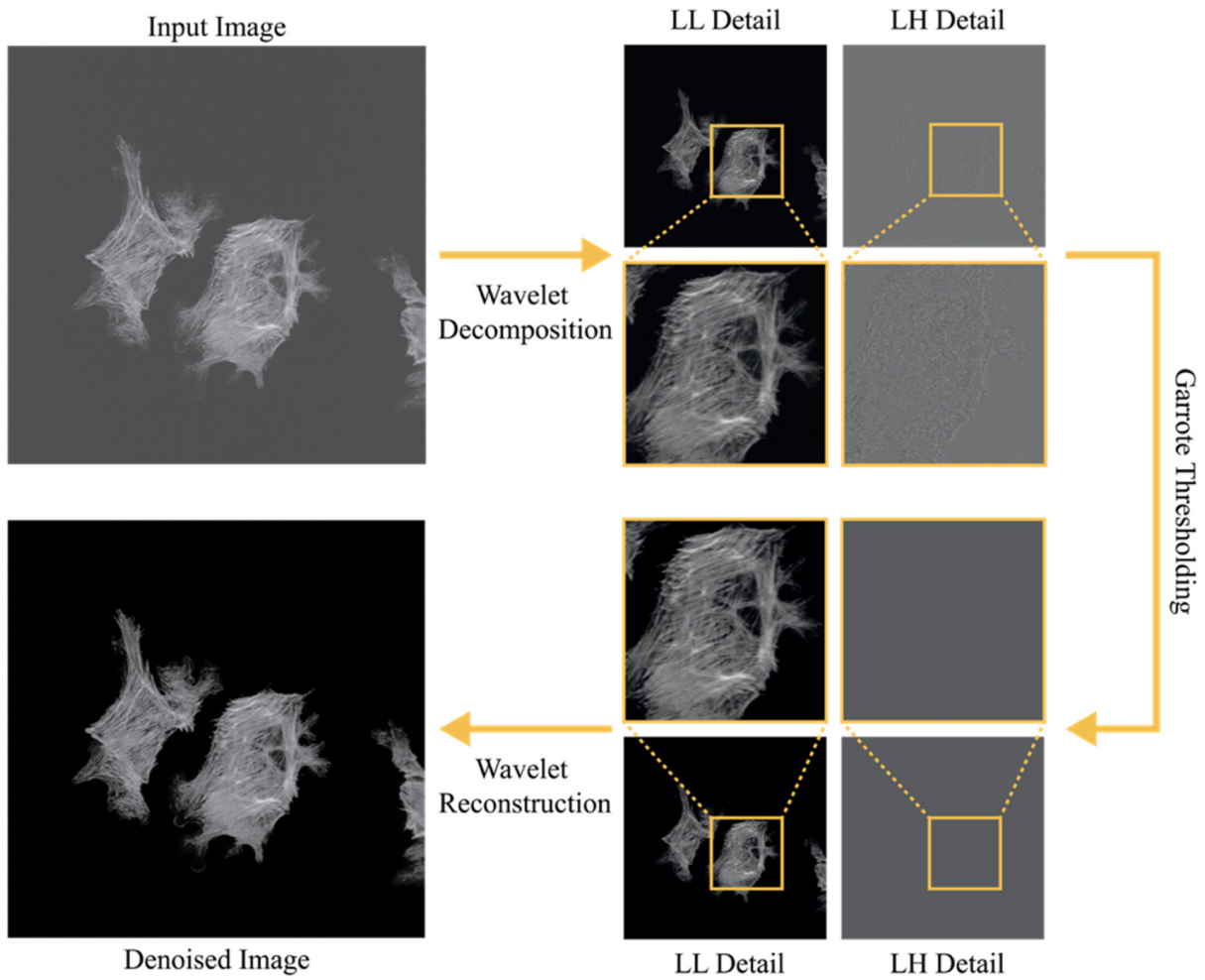
FIGURE 4 | Illustration of the denoising process applied to fluorescence microscopy image, highlighting the use of Haar wavelet transform for effective noise reduction and detail retention in the LL and LH sub-images.

$$I_{sharp} = I + \eta \times (I - I_{blur}) \quad (10)$$

where I_{sharp} is the sharpened image, I is the original denoised image, I_{blur} is a blurred version of the original image obtained by applying a 3×3 Gaussian blur filter, and η is a user-defined parameter called the sharpening factor that controls the degree of sharpening applied. Higher values of η result in more pronounced sharpening, while lower values provide a more subtle enhancement. However, it is important to find a balance when setting the η value to avoid introducing unnatural graininess or halos around edges, which can occur when the sharpening effect is too strong. To ensure an optimal edge contrast enhancement while maintaining a natural appearance, we carefully tuned the η value for each dataset through the hyperparameter tuning process described in Section 3.1. Figure 5 illustrates the sharpening effect of this step on the denoised image.

2.5 | Autofluorescence Correction

In fluorescence imaging, particularly during 3D acquisitions, autofluorescence emanating from surrounding structures can obstruct the clear signals from the primary targets of interest. This autofluorescence essentially comprises intrinsic fluorescence that is unrelated to the introduced fluorophores. Our innovative algorithm addresses this issue through pixel-wise brightness calibration, aiming to significantly reduce the interference caused by autofluorescence. While the method can be applied to various fluorescent structures, such as cell membranes or organelles, we will use the example of nuclei fluorescence for illustration purposes. The correction strategy includes the following phases:

1. Autofluorescence detection: initially, segmentation masks were generated using a ConvNeXt neural network [24] to isolate regions of interest (ROI), specifically cell nuclei, from background areas. This step helps distinguish between the intended fluorescence signal and areas potentially exhibiting autofluorescence. A detailed description of the model architecture, training parameters, and configuration can be found in Data S1.

2. Autofluorescence isolation: following the generation of ROI segmentation masks, we distinguish the fluorescent structure information from the autofluorescence signals. This is accomplished by applying the mask to the analyzed image, which isolates only the recognized ROI. Conversely,
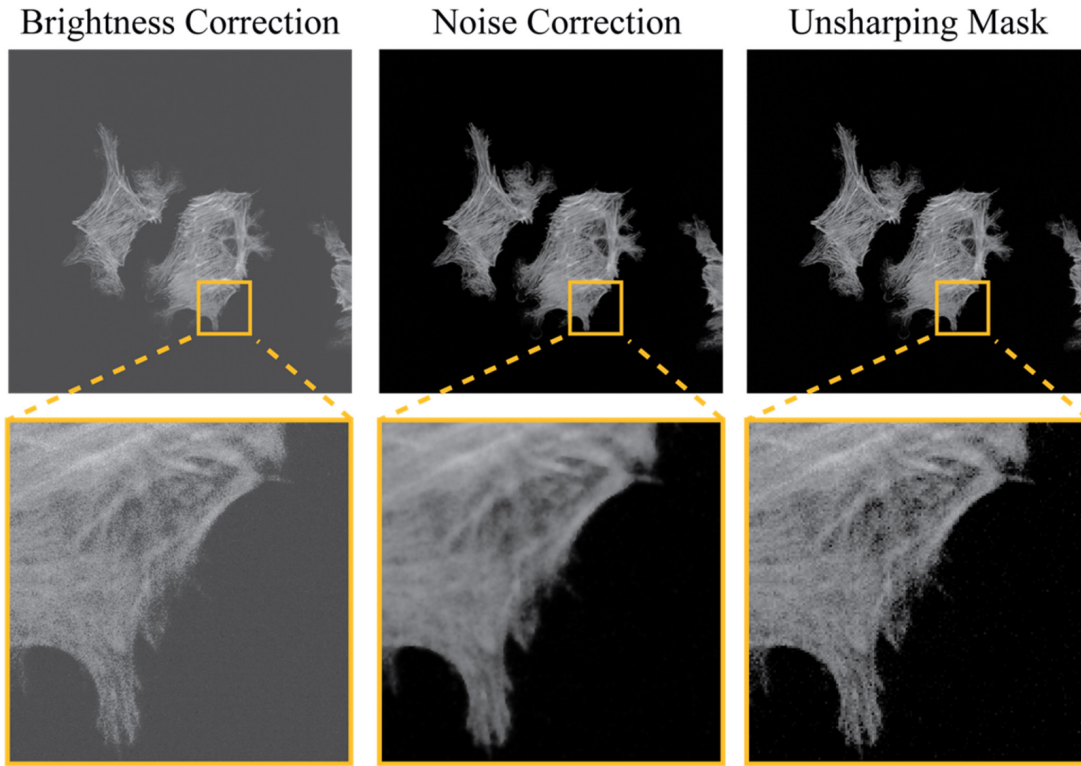
FIGURE 5 | Comparative display of different processing stages: Brightness correction, noise correction, and unsharp masking. Zoomed sections beneath each stage highlight the detail retrieval accomplished through unsharp masking following noise correction.

utilizing the inverse of the mask allows us to exclusively isolate the areas exhibiting autofluorescence.

$$I_{\text{autofluo}} = I \times \left(1 - \text{mask}_{\text{ROI}}\right) \tag{11}$$

$$I_{\text{ROI}} = I \times \text{mask}_{\text{ROI}} \tag{12}$$

This facilitated independent modulation of autofluorescence while preserving the original characteristics of the fluorescent structures.

3. Autofluorescence modulation: the aim of this step is to enhance the visibility of the desired fluorescent structures. Specifically, we seek to reduce the intensity of pixels associated with autofluorescence, while concurrently amplifying the intensity of ROI pixels that are inaccurately segmented and submerged within the autofluorescence regions. To facilitate this selective enhancement of the $I_{\text{autofluorescence}}$, two distinct thresholds are established, based on linear combinations of the average brightness values from both nuclei and autofluorescence, respectively:

$$T_{\text{autofluo}} = w_1 \times \mu\left(I_{\text{ROI}}\right) + w_2 \times \mu\left(I_{\text{autofluo}}\right) \tag{13}$$

$$T_{\text{ROI}} = w_3 \times \mu\left(I_{\text{ROI}}\right) + w_4 \times \mu\left(I_{\text{autofluo}}\right) \tag{14}$$

It is important to note that $w_1, w_2, w_3,$ and w_4 are fixed parameters with values of 0.15 and 0.85 for w_1 and w_2 and 0.9 and 0.1 for w_3 and w_4, respectively. The relationships $w_2 > w_1$, and $w_3 > w_4$ ensure that the threshold for autofluorescence

(T_{autofluo}) is higher than the average intensity of the ROI, while the threshold for the ROI (T_{ROI}) is lower than the average intensity of the autofluorescence.

Once the intervals are defined using the computed thresholds, we proceed to modulate pixel intensities within the I_{autofluo} image. This selective modulation is achieved using the following linear transformations:

$$\begin{cases} \alpha_1 x & 0 < x \le T_{\text{autofluo}} \\ \beta_1\left(x - T_{\text{autofluo}}\right) + T'_{\text{autofluo}} & T_{\text{autofluo}} < x \le T_{\text{ROI}} \\ \gamma_1\left(x - T_{\text{ROI}}\right) + T'_{\text{ROI}} & T_{\text{ROI}} < x \le 255 \end{cases} \tag{15}$$

The slope coefficients for these linear transformations are given as follows:

$$\alpha_1 = \frac{T'_{\text{autofluo}}}{T_{\text{autofluo}}}$$

$$\beta_1 = \frac{T'_{\text{nuclei}} - T'_{\text{autofluo}}}{T_{\text{nuclei}} - T_{\text{autofluo}}}$$

$$\gamma_1 = \frac{255 - T'_{\text{ROI}}}{255 - T_{\text{ROI}}} \tag{16}$$

The terms T'_{nuclei} and T'_{autofluo} represent the modulated thresholds, and are defined as:

$$T'_{\text{autofluo}} = \delta_{\text{autofluo}} \times T_{\text{autofluo}} \tag{17}$$

$$T'_{\mathrm{ROI}} = \varepsilon_{\mathrm{ROI}} \times T_{\mathrm{ROI}} \qquad (18)$$

where $\delta_{\mathrm{autofluo}}$ and $\varepsilon_{\mathrm{nuclei}}$ are user-defined parameters ranging between 0 and 1, that represent the autofluorescence reduction factor and the nuclei amplification factor, respectively. $\delta_{\mathrm{autofluo}}$ is a value that has been configured in such a way as to significantly reduce the visual effect of autofluorescence in the area, while still preserving minimal visibility of the surrounding structure from which interferences arises. On the other hand, $\varepsilon_{\mathrm{ROI}}$ has been set to discreetly increase the brightness of objects erroneously not recognized as nuclei during segmentation, although these parameters can be adjusted depending in the desired final correction effect.

Through adjustment of the modulation parameters, we can precisely suppress autofluorescence, leading to enhanced clarity and contrast, especially in the representation of nuclear targets. Figure 6a offers a comprehensive visualization of the entire autofluorescence correction process, while Figure 6b demonstrates the outcomes of autofluorescence suppression achieved by varying the value of $\delta_{\mathrm{autofluo}}$ showcasing the effects of different magnitudes of suppression. After the modulation, I_{autofluo} is merged back with I_{nuclei} to produce a fluorescence microscopy image characterized by enhanced contrast and minimized autofluorescence interference.

2.6 | Performance Evaluation

We conducted all quantitative analyses and comparisons using the processed grayscale images. For visual representation and qualitative assessment, however, we reapplied the original color-coding of each fluorescence channel to these processed images. This approach presents enhanced images that retain the visual appearance of fluorescence microscopy data while highlighting the improvements achieved through our processing methods.

To validate the efficiency of our algorithm, we employed a comprehensive approach, including multiple evaluation metrics. Firstly, we assessed the algorithm's ability to improve image contrast using the Contrast Improvement Index (CII) [25] across all datasets. A CII score greater than 1 indicates significant contrast enhancement, highlighting our objective of enhancing faintly visible objects and reducing noise.

For the dataset from Hagen et al. where high-SNR versions were available as a benchmark, we utilized full-reference evaluation metrics. These included the PSNR [26], Structural Similarity Index (SSIM) [27], and the Multi-Scale Structural Similarity Index (MS-SSIM) [28]. MS-SSIM measures perceptual similarity between processed and original images, with scores ranging from 0 to 1. A score of 1 signifies perfect similarity, validating the proficiency in artifact rectification while preserving semantic content.

To evaluate the effectiveness of our autofluorescence correction method, we assessed the SNR [29] of processed images using manual masks for datasets containing autofluorescence (cardiosphere). We considered varying levels of correction (25%, 50%, and 100%) to analyze the impact on SNR.

Finally, to evaluate the potential utility of our method in deep learning contexts, we trained multiple segmentation networks on original images and images processed with both traditional methods (BM3D, CLAHE), a deep learning-based denoising method (CARE [30]), and our approach. Performance was assessed using the Dice Score [31], Aggregate Jaccard Index (AJI) [32], Panoptic Quality (PQ) [33], and Hausdorff Distance (HD) [34].

3 | Results

3.1 | Hyperparameter Tuning

To optimize the performance of our algorithm across different datasets, it was essential to finetune specific hyperparameters. Given the variability in image characteristics among datasets, a uniform set of parameters might not yield the best outcomes universally. Therefore, we conducted a hyperparameter tuning process to identify the optimal set of parameters tailored for each dataset. The tuning process involved a systematic exploration of the parameter space, guided by both quantitative metrics and qualitative visual assessment. For each dataset, we evaluated the algorithm's performance using a range of parameter values and selected the combination that maximized the CII while preserving important image details and minimizing artifacts. The key parameters tuned in this process were the offset values ($\mathrm{offset}_{\mathrm{dark-mid}}$, $\mathrm{offset}_{\mathrm{dark}}$, $\mathrm{offset}_{\mathrm{mid}}$), which control the tonal interval boundaries, the denoising factor (D) and the sharping degree (η). The optimal values for these parameters vary across datasets due to differences in image contrast, noise levels, and the presence of specific structures or features. Table 2 presents the best-performing hyperparameters identified for each dataset during the tuning process.

3.2 | Comparison With Heuristic Methods

In this section, we analyze and compare the results of our proposed algorithm against two established techniques: BM3D and CLAHE. We evaluate the image quality in terms of clarity, contrast, and detail preservation.

Figure 7 demonstrates that our method performs well, especially on low SNR images of actin and mitochondria. The enhanced images closely match their original high SNR counterparts, outperforming the other methods. This consistency is maintained regardless of the image content (actin vs. mitochondria) or magnification level (20× vs. 60×). Figure 7b presents additional results on cardiosphere images. Our technique effectively increases contrast without amplifying artifacts, an issue observed with CLAHE. Moreover, it selectively accentuates cell visibility for a clear representation, unlike the other techniques. Additional visual comparisons with traditional image enhancement techniques are reported in the Data S1.

Figure 8 provides a quantitative evaluation of our method on the actin and mitochondria dataset. For the CII metric, our method consistently scores higher than other techniques across all subsets, with an improvement compared to the LowSNR images of 132.63% for the Actin20x subset, 125.54% for Actin60, 238.66% for Mito20x, and 299.84% for Mito60x.

(a)

(b)
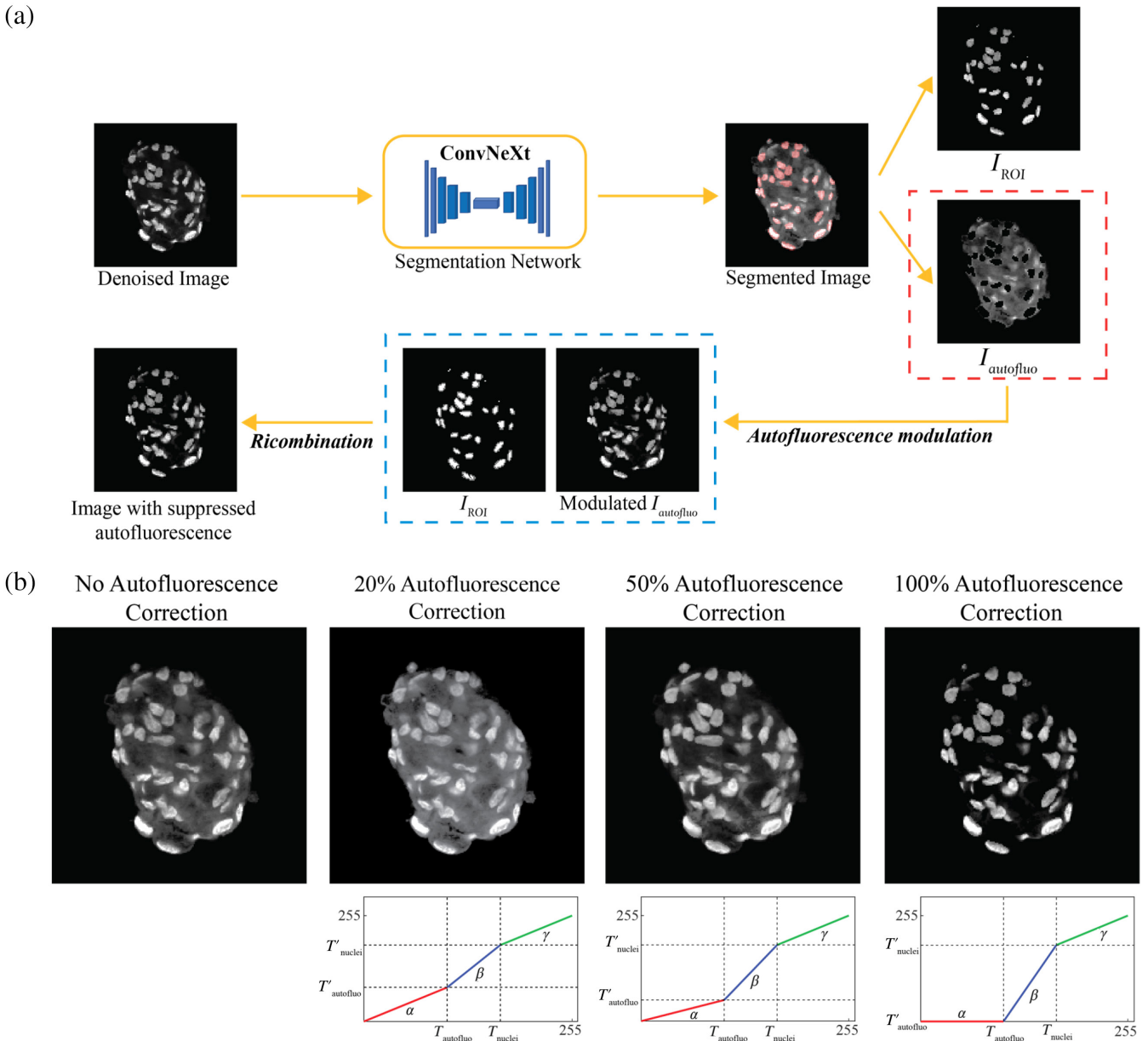
FIGURE 6 | Autofluorescence correction overview and comparison. (a) Schematic representation detailing the entire autofluorescence correction process. (b) Demonstrative images of a cardiosphere processed with distinct levels of autofluorescence reduction: 20%, 50%, and 100%. The images highlight the progressive clarity in nuclear target depiction (bright areas) with increasing suppression of autofluorescence. The gray background represents a combination of cellular cytoplasm and extracellular matrix, which together form the structure of the cardiosphere.

In terms of the PSNR score, our method demonstrates higher values compared to other techniques. The increase in PSNR is 40.39% for the Actin20x subset, 40.95% for Actin60x, 48.86% for Mito20x, and 19.60% for Mito60x. Finally, when evaluating the preservation of image content, our method achieves the highest scores in both SSIM and MS-SSIM metrics, indicating its superiority in maintaining the structural integrity of the enhanced images.

Figure 9 presents the mean scores for the CII metric on the cardiosphere images, comparing the performance of BM3D, CLAHE, and our method. The results underscore the effectiveness of our approach in this domain. Specifically, our method achieves a score of 3.33, significantly outperforming BM3D,

which obtains a score of 0.43, and CLAHE, which yields a score of 1.33.

3.3 | Comparison With Deep Learning Methods

In this section, we compare the results of our proposed algorithm with the CARE method, a powerful deep learning approach for image enhancement. Figure 10a presents a bar graph of the mean CII values with standard deviations for each subset, comparing the performance of our method against CARE. The results demonstrate that our method consistently achieves higher CII values compared with CARE, indicating superior contrast enhancement and detail preservation.
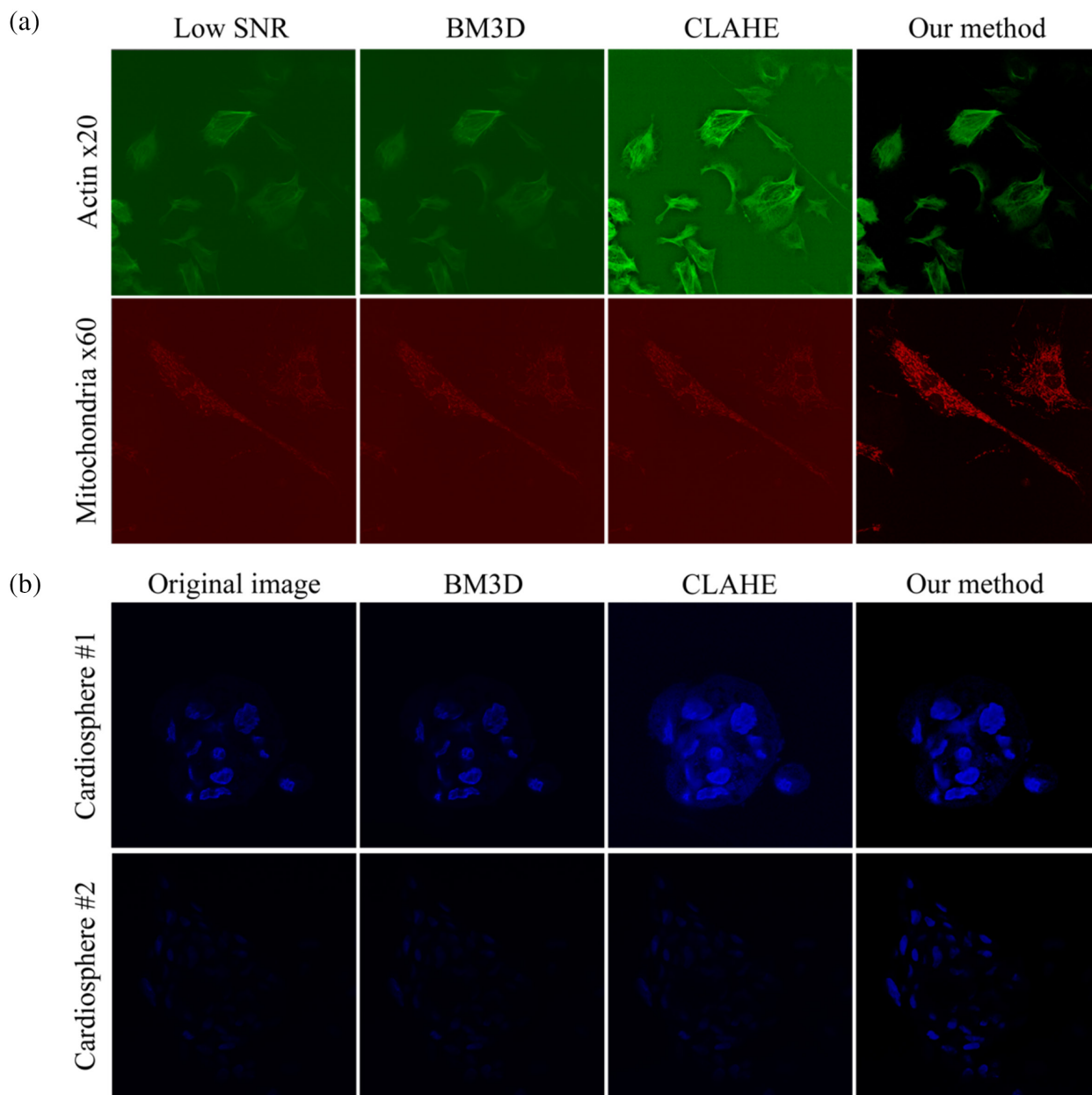
FIGURE 7 | Visual illustration showcasing the enhancement capabilities of our method versus BM3D [12] and CLAHE [13] algorithms, for (a) actin and mitochondria images and (b) cardiosphere images.

For instance, in the Actin20x subset, our method achieves an average CII of 1.54 (±0.20) compared to CARE's 0.80 (±0.09), nearly doubling the contrast improvement. In the Actin60x subset, our method scores 1.70 (±0.46) against CARE's 0.94 (±0.10), showing a significant enhancement in image quality. Similarly, for the Mito20x subset, our method achieves a CII of 1.91 (±0.11), markedly higher than CARE's 0.68 (±0.16). Finally, in the Mito60x subset, our method scores 1.72 (±0.26), compared with 1.14 (±0.13) obtained by CARE, demonstrating superior performance in preserving image details and enhancing contrast.

Figure 10b presents visual examples from the Actin20x, Actin60x, Mito20x, and Mito60x subsets, showcasing the original LowSNR images, images processed with CARE, and images processed with our method. The visual comparisons further illustrate the advantages of our approach over CARE, highlighting the improved contrast, clarity, and detail preservation achieved by our method.

3.4 | Autofluorescence Correction

In this section, we examine the efficacy of our algorithm's autofluorescence correction function. Figure 11a offers a qualitative demonstration of the autofluorescence correction at various intensities. The progression from 25% to 100% correction showcases a significant improvement in the reduction of autofluorescence, with the corrected images displaying a decrease in unwanted fluorescence as the correction level increases.
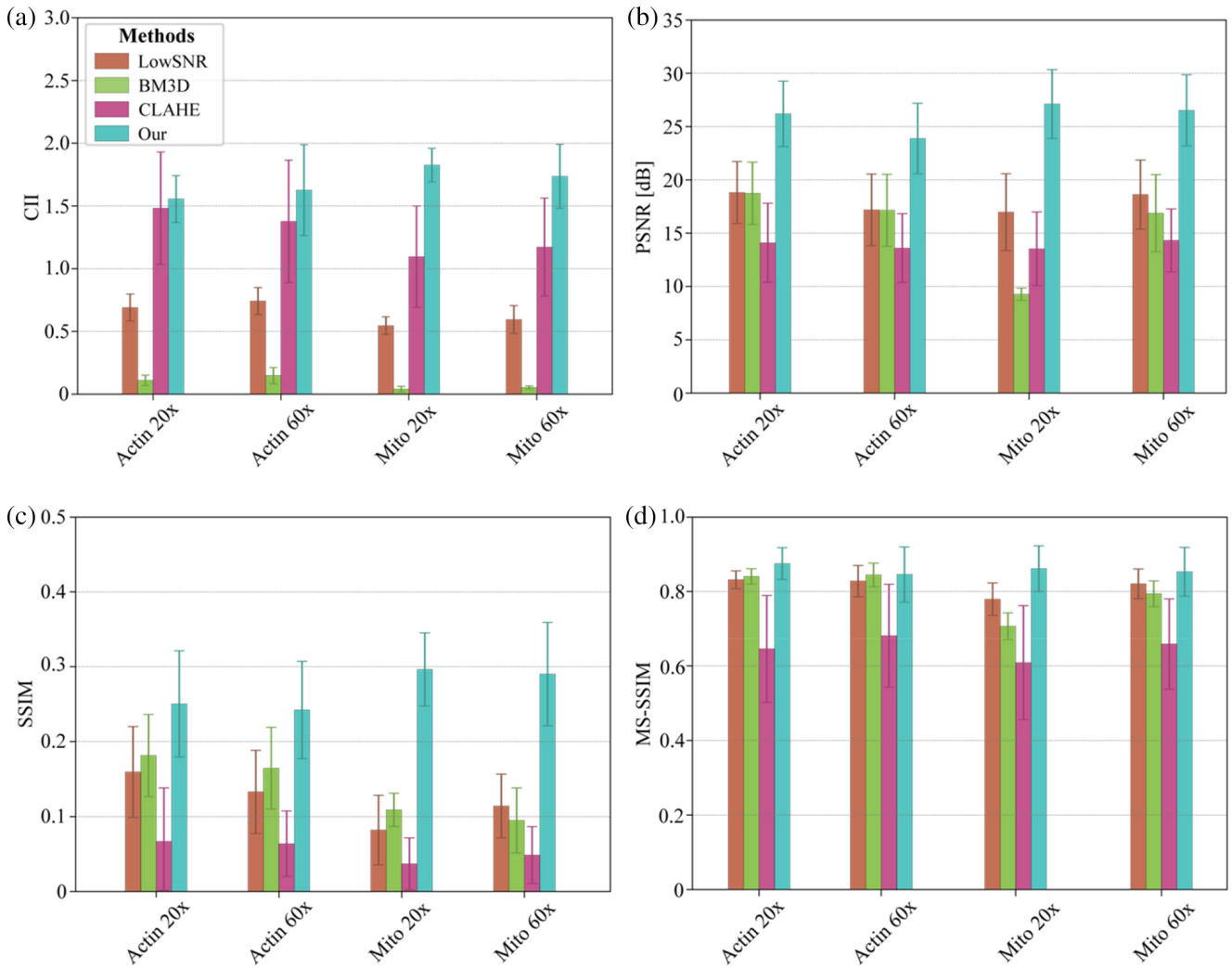
FIGURE 8 | Quantitative comparison of our method with BM3D and CLAHE algorithms on different subsets of the Hagen et al. dataset, with reference metrics calculated relative to the HighSNR versions. Each panel represents a different evaluation metric: (a) CII [25], (b) PSNR [26], (c) SSIM [27], and (d) MS-SSIM [28]. Each tick denotes a distinct subset within the dataset.
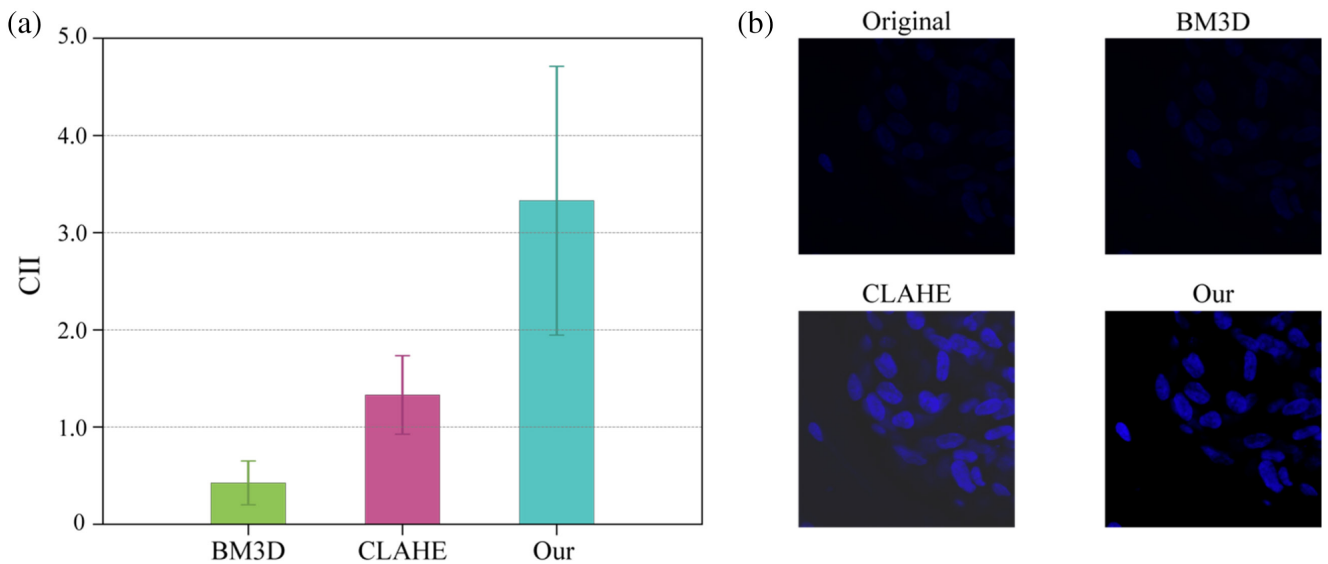
FIGURE 9 | Comparison of image enhancement methods for the cardiosphere dataset. (a) Bar plot comparison of the CII values for the cardiosphere dataset using different methods. Each bar represents the performance of the respective method. (b) Visual example of the same cardiosphere image in its original version and processed with BM3D, CLAHE, and our method.
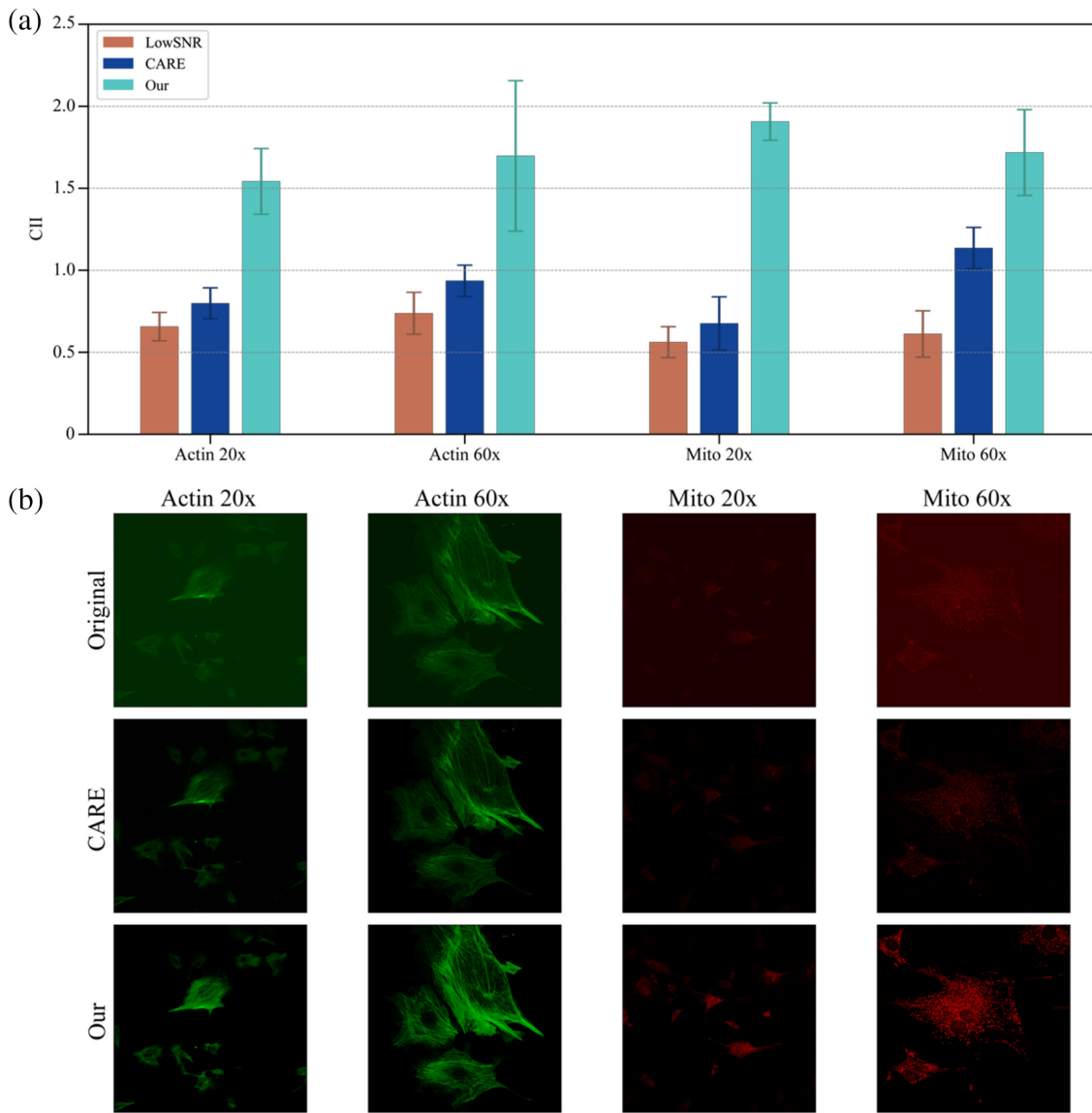
FIGURE 10 | Comparison of our method with CARE (a) bar graph showing the mean Contrast Improvement Index (CII) values with standard deviations for each subset (b) visual examples from each subset, showing the original LowSNR images, images processed with CARE, and images processed with our method.

Figure 11a provides a comparative quantitative analysis of SNR values to evaluate the performance of our autofluorescence correction method. The original images have an SNR of 12 dB. When our method is applied with a 25% correction, the SNR slightly decreases to 11.4 dB, which is a marginal reduction of approximately 4.6% from the original. At a 50% correction level, our method surpasses the original with an SNR of 12.8 dB, demonstrating an improvement of approximately 6.6%. The most notable enhancement is achieved with a 100% correction, where the SNR reaches 15 dB, indicating a substantial increase of 24.7% over the original SNR value.

In comparison, BM3D exhibits a negligible improvement, with an SNR value of 12 dB, showing a slight increase of 0.1% from the original. CLAHE, conversely, results in a significant SNR decrease to 6.6 dB, which is a reduction of 44.9% compared with the original images.

In addition to these quantitative metrics, the corrected images were subjected to expert qualitative assessment. A domain expert in fluorescence microscopy (T.P.) visually evaluated the processed images. The analysis confirmed that the method effectively suppresses autofluorescence while maintaining the visibility and integrity of the cellular structures of interest, particularly the cell nuclei (Figure 11b).

3.5 | Impact on an AI-Segmentation Framework

This section presents the testing results obtained from AI-based segmentation frameworks trained using images processed with different methods. We employed a ConvNeXt-based UperNet model [35] for semantic segmentation. The backbone, initialized with pretrained weights from the ADE20K dataset [36], extracts multi-scale feature maps that are fed into the decode head to
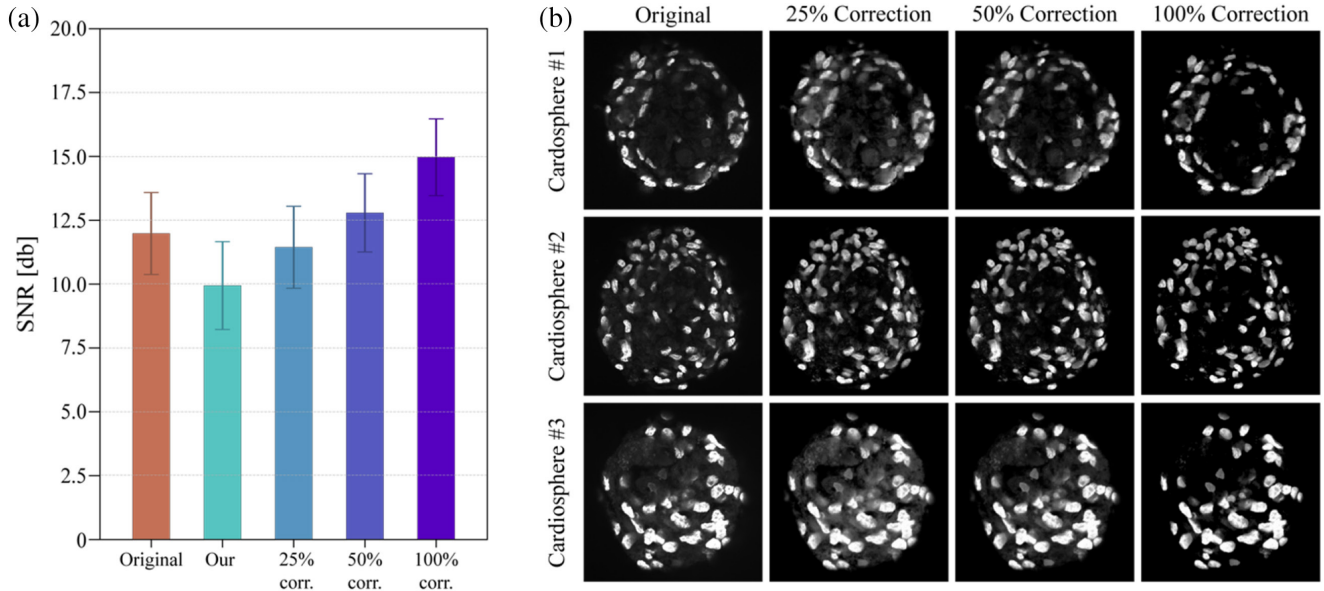
FIGURE 11 | Qualitative and quantitative evaluation of autofluorescence correction. (a) Quantitative analysis based on SNR values. (b) Qualitative assessment showcasing the autofluorescence correction capability at different levels: 25% (second column), 50% (third column), and 100% (fourth column). Images are represented in grayscale to better evaluate the effect of autofluorescence correction.

TABLE 3 | Performance metrics on AI-based segmentation frameworks trained using images processed with different methods.

Method	Dice	AJI	PQ	HD
Original image	0.8165 ± 0.065	0.6291 ± 0.091	0.6262 ± 0.045	5.52 ± 0.98
CLAHE	0.8184 ± 0.052	0.6304 ± 0.085	0.6260 ± 0.039	5.69 ± 0.81
BM3D	0.7896 ± 0.081	0.5892 ± 0.104	0.5510 ± 0.057	5.43 ± 1.06
CARE	0.8198 ± 0.057	0.6306 ± 0.074	0.6291 ± 0.031	5.32 ± 0.59
Our method	$\mathbf{0.8214 \pm 0.031}$	$\mathbf{0.6396 \pm 0.055}$	$\mathbf{0.6327 \pm 0.026}$	$\mathbf{4.99 \pm 0.47}$

Abbreviations: AJI: Aggregated Jaccard Index, Dice: Dice similarity coefficient, HD: Hausdorff distance, PQ: Panoptic quality.
Note: Bold font was employed to highlights the best results.

produce segmentation maps with three classes: background, cell border, and inner area. An auxiliary head provides additional supervision during training. The model was trained using an AdamW optimizer with a learning rate of 0.0001, weight decay of 0.05, and a polynomial learning rate schedule with linear warmup. The training was conducted on a GeForce RTX 3090 GPU with a batch size of four images per GPU for 50 epochs. As a post-processing step, we applied the same strategy proposed in our previous works [37, 38], to obtain the instance segmentation of cell nuclei.

Our method achieves the highest Dice score for the segmentation task among all the compared methods (Table 3). In terms of the AJI metric, our method shows an enhancement of 1.67%, which is higher than the increment in CLAHE (0.21%) and outperforms BM3D's decline of 6.35%. For the PQ score, our method demonstrates a growth of 1.04%, while CLAHE essentially remains consistent with a decrement of 0.03%, and BM3D exhibits a decline of 12.00%. Finally, regarding the HD metric, our method yields the most significant improvement, decreasing the score by 9.60%, compared with CLAHE's increment of 3.08% and BM3D's decrement of 1.63%.

4 | Discussion

Fluorescence microscopy, despite its extensive applications in biological and medical research, often suffers from limitations such as low contrast [5], high noise levels [6], and unwanted autofluorescence [8, 9]. These factors are largely due to the inherent limitations in the quality of the data acquired, which is critical for fluorescence analysis. High-quality acquisitions can be compromised by noise from instrumentation and the delicate nature of the samples, which cannot be exposed to high-intensity optical sources. These issues can significantly hinder the interpretation and analysis of microscopy images, impacting the reliability of research outcomes.

Our study introduces a novel heuristic algorithm that substantially improves image quality by enhancing contrast, reducing noise, and, with the help of AI, correcting autofluorescence in fluorescence microscopy images. The algorithm's effectiveness is demonstrated through extensive quantitative and qualitative comparisons on diverse datasets, showing notable advancements over existing methods like BM3D and CLAHE. Our method demonstrated a remarkable increase in

the CII for the Actin and Mito datasets, with enhancements of 132.63% for Actin20x, 125.54% for Actin60x, 238.66% for Mito20x, and 299.84% for Mito60x compared to LowSNR images. Furthermore, for the cardiosphere dataset, our approach significantly outperformed others, achieving a CII score of 3.01 against scores of 0.56 by BM3D and 1.33 by CLAHE, highlighting the superior capability of our algorithm in enhancing the data quality critical for accurate fluorescence microscopy analysis.

Preserving the essential details and information in images is of prime importance, and our method has shown superior performance compared with the other methods. For the actin and mitochondria dataset, which had high-quality counterparts for reference, our algorithm recorded a substantial rise in the PSNR: 40.39% for Actin20x, 40.95% for Actin60x, 48.86% for Mito20x, and 19.60% for Mito60x. This indicates a significant reduction in noise while maintaining the sharpness and clarity of the images. Moreover, our method achieved the highest scores in terms of the SSIM and MS-SSIM, evidencing its ability to retain and even enhance the informational content of the images.

Based on the autofluorescence correction task, our algorithm achieved a 24.69% improvement over the original SNR value for the maximum level of autofluorescence correction. These metrics, presented in Table 3, illustrate the algorithm's ability to support human interpretation and improve deep learning frameworks.

Our proposed method demonstrates remarkable versatility across various fluorescence microscopy applications. Its heuristic nature eliminates the need for manual segmentation or extensive training to achieve higher quality images, thereby simplifying the preprocessing pipeline for microscopy images.

Figure 12 illustrates this adaptability by showcasing the method's effectiveness in processing both multi-channel and three-dimensional data. Currently, the algorithm operates on and processes single 2D channels. For multi-channel images (Figure 12a), each channel is processed separately, and the results are then recombined to produce the final enhanced image. In the case of 3D data, the algorithm processes each slice independently before aggregating the results into an enhanced 3D reconstruction, as demonstrated in Figure 12b.

Despite its effective performance, our method has some limitations that should be acknowledged. Firstly, the algorithm requires fine-tuning of parameters for optimal performance across different applications and datasets (Table 2). This need for customization may limit its immediate applicability to new, unseen data without initial adjustment. Second as a mathematical-based approach, our method has slightly longer computational times compared to deep learning-based solutions (0.14 s vs. 0.10 s per image), particularly for high-resolution images. Additionally, for multi-channel data, the method currently processes each channel independently, which may not fully leverage potential correlations between channels.

While our approach shows promising results on 2D single-channel images, there are opportunities to extend its capabilities. Future work could expand the methodology to operate on 3D volumetric acquisitions as well as multichannel images like those from immunofluorescence microscopy. This would allow it to be applied to additional imaging modalities that produce these data types, such as photoacoustic microscopy. Additionally, developing a fully integrated method that performs fluorescent signal extraction and enhancement simultaneously could streamline the process.
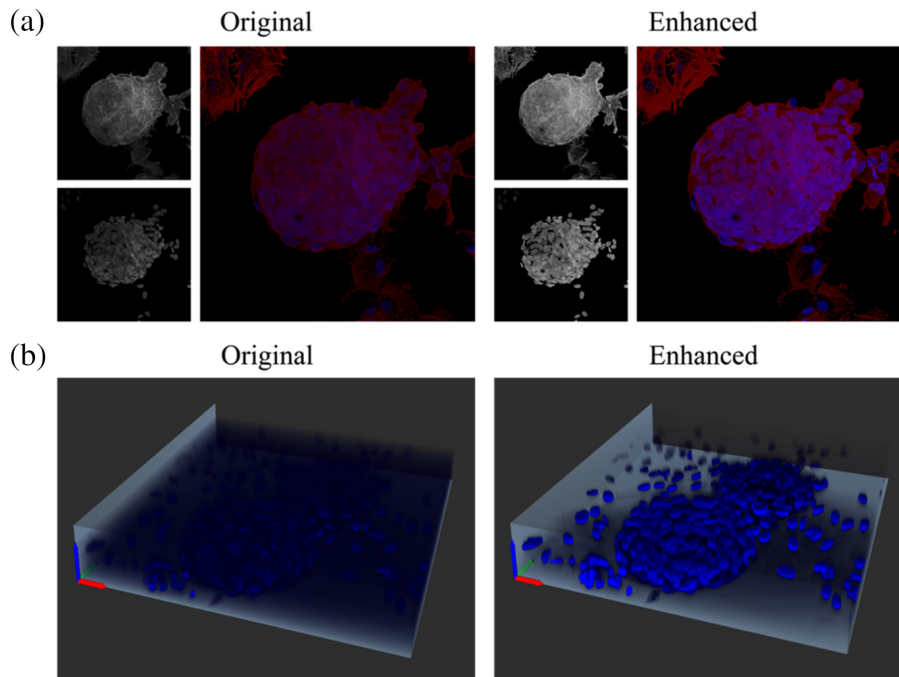
FIGURE 12 | Versatility of the proposed method on different fluorescent data. (a) Multi-channel image enhancement: original (left) and processed (right) images, showing separate enhancement of individual channels before recombination. (b) Three-dimensional reconstruction of a cardiosphere sample: original 3D image compared to the enhanced counterpart after applying the proposed pipeline to each 2D slice independently.

5 | Conclusions

In conclusion, our novel algorithm has demonstrated significant improvements in image quality for fluorescence microscopy by enhancing contrast, reducing noise, and correcting autofluorescence. Comprehensive evaluation across diverse datasets reveals the superior performance of this method over existing techniques, with substantial improvements in quantitative metrics. The modular design of our algorithm allows the processing of multi-channel data and, in the future, also three-dimensional data. The improvement of fluorescence images has the potential to advance both basic research and clinical applications, contributing to more precise studies in cell biology and medical diagnostics.

Author Contributions

F.B. proposed the algorithm, designed the experiments and wrote the first draft of the manuscript. M.M. coded the algorithm and applied it to the dataset used in this study. K.M.M. and T.P. reviewed the manuscript. M.S. supervised the study and revised the manuscript.

Ethics Statement

The authors have nothing to report.

Consent

The authors have nothing to report.

Conflicts of Interest

The authors declare no conflicts of interest.

Data Availability Statement

The datasets during the current study are publicly available: actin and mitochondria images (DOI: 10.1093/gigascience/giab032); cardiosphere data (DOI: 10.17632/tntrkg27st.2). The source code of the proposed algorithm is available from the corresponding author on reasonable request.

References

1. C. A. Combs, "Fluorescence Microscopy: A Concise Guide to Current Imaging Methods," *Current Protocols in Neuroscience* 50, no. 1 (2010): 2.1.

2. G. P. C. Drummen, "Fluorescent Probes and Fluorescence (Microscopy) Techniques-Illuminating Biological and Biomedical Research," *Molecules* 17 (2012): 14067–14090.

3. S. Seoni, A. Shahini, K. M. Meiburger, et al., "All You Need Is Data Preparation: A Systematic Review of Image Harmonization Techniques in Multi-Center/Device Studies for Medical Support Systems," *Computer Methods and Programs in Biomedicine* 250 (2024): 108200.

4. B. Huang, M. Bates, and X. Zhuang, "Super-Resolution Fluorescence Microscopy," *Annual Review of Biochemistry* 78 (2009): 993–1016.

5. S. Acuña, M. Roy, L. E. Villegas-Hernández, V. K. Dubey, B. S. Ahluwalia, and K. Agarwal, "Deriving High Contrast Fluorescence Microscopy Images Through Low Contrast Noisy Image Stacks," *Biomedical Optics Express* 12, no. 9 (2021): 5529–5543.

6. V. Mannam, Y. Zhang, Y. Zhu, et al., "Real-Time Image Denoising of Mixed Poisson–Gaussian Noise in Fluorescence Microscopy Images Using ImageJ," *Optica* 9, no. 4 (2022): 335.

7. M. J. Sanderson, I. Smith, I. Parker, and M. D. Bootman, "Fluorescence microscopy," *Cold Spring Harbor Protocols* 2014, no. 10 (2014): 1042–1065.

8. N. M. Cordina, N. Sayyadi, L. M. Parker, A. Everest-Dass, L. J. Brown, and N. H. Packer, "Reduced Background Autofluorescence for Cell Imaging Using Nanodiamonds and Lanthanide Chelates," *Scientific Reports* 8, no. 1 (2018): 4521.

9. J. R. Mansfield, K. W. Gossage, C. C. Hoyt, and R. M. Levenson, "Autofluorescence Removal, Multiplexing, and Automated Analysis Methods for In-Vivo Fluorescence Imaging," *Journal of Biomedical Optics* 10, no. 4 (2005): 041207.

10. S. M. Hickey, B. Ung, C. Bader, et al., "Fluorescence Microscopy – An Outline of Hardware, Biological Handling, and Fluorophore Considerations," *Cells* 11 (2022): 35.

11. E. H. K. Stelzer, "Contrast, Resolution, Pixelation, Dynamic Range and Signal-To-Noise Ratio: Fundamental Limits to Resolution in Fluorescence Light Microscopy," *Journal of Microscopy* 189, no. 1 (1998): 15–24.

12. M. Lebrun, "An Analysis and Implementation of the BM3D Image Denoising Method," *Image Processing on Line* 8, no. 2 (2012): 175–213.

13. G. S. Omarova, A. Zhzh, and V. Starovoitov, "Application of the Clahe Method Contrast Enhancement of X-Ray Images," *International Journal of Advanced Computer Science and Applications* 13, no. 5 (2022): 412–420, www.ijacsa.thesai.org.

14. M. Casper, H. Schulz-Hildebrandt, M. Evers, R. Birngruber, D. Manstein, and G. Hüttmann, "Optimization-Based Vessel Segmentation Pipeline for Robust Quantification of Capillary Networks in Skin With Optical Coherence Tomography Angiography," *Journal of Biomedical Optics* 24, no. 4 (2019): 1–11.

15. T. M. Khan, M. A. U. Khan, N. U. Rehman, et al., "Width-Wise Vessel Bifurcation for Improved Retinal Vessel Segmentation," *Biomedical Signal Processing and Control* 1 (2022): 71.

16. K. Naveed, F. Abdullah, H. A. Madni, M. A. U. Khan, T. M. Khan, and S. S. Naqvi, "Towards Automated Eye Diagnosis: An Improved Retinal Vessel Segmentation Framework Using Ensemble Block Matching 3D Filter," *Diagnostics* 11, no. 1 (2021): 114.

17. G. F. C. Campos, S. M. Mastelini, G. J. Aguiar, R. G. Mantovani, L. F. de Melo, and S. Barbon, "Machine Learning Hyperparameter Selection for Contrast Limited Adaptive Histogram Equalization," *EURASIP Journal on Image and Video Processing* 2019, no. 1 (2019): 59.

18. G. M. Hagen, J. Bendesky, R. Machado, T. A. Nguyen, T. Kumar, and J. Ventura, "Fluorescence Microscopy Datasets for Training Deep Neural Networks," *GigaScience* 10, no. 5 (2021): 1–6.

19. M. Salvi, U. Morbiducci, F. Amadeo, et al., "Automated Segmentation of Fluorescence Microscopy Images for 3D Cell Detection in Human-Derived Cardiospheres," *Scientific Reports* 9, no. 1 (2019): 6644.

20. A. Mohsin Abdulazeez, D. Q. Zeebaree, D. A. Zebari, G. M. Zebari, I. Mohammed, and N. Adeen, "Journal of Soft Computing and Data Mining the Applications of Discrete Wavelet Transform in Image Processing: A Review," *Journal of Soft Computing and Data Mining* 1, no. 2 (2020): 31–43, http://penerbit.uthm.edu.my/ojs/index.php/jscdm.

21. X. Zhixi and Institute of Electrical and Electronics Engineers, "ICEOE 2011: 2011 International Conference on Electronics and Optoelectronics," in *Proceedings IEEE* (Dalian, China: IEEE, 2011), 29–31.

22. B. Dehda and K. Melkemi, "Image Denoising Using New Wavelet Thresholding Function," *Journal of Applied Mathematics and Computational Mechanics* 16, no. 2 (2017): 55–65.

23. G. Deng, "A Generalized Unsharp Masking Algorithm," *IEEE Transactions on Image Processing* 20, no. 5 (2011): 1249–1261.

24. Z. Han, M. Jian, and G. G. Wang, "ConvUNeXt: An Efficient Convolution Neural Network for Medical Image Segmentation," *Knowledge-Based Systems* 11 (2022): 253.

25. K. Rao, A. Agarwal, and S. Dhall, "Contrast Enhancement Techniques: A Survey," *International Journal of Signal Processing, Image Processing and Pattern Recognition* 10, no. 12 (2017): 35–62.

26. A. Horé and D. Ziou, "Image Quality Metrics: PSNR vs. SSIM," in *Proceedings International Conference on Pattern Recognition* (2010), 2366–9.

27. Institute of Electrical and Electronics Engineers, "IEEE Signal Processing Society. ICIP," in *IEEE International Conference on Image Processing* (San Diego, California, USA: IEEE, 2008).

28. Z. Wang, E. P. Simoncelli, and A. Bovik, "Multi-Scale Structural Similarity for Image Quality Assessment," 2003.

29. Institute of Electrical and Electronics Engineers, "IEEE Instrumentation and Measurement Society," in *Proceedings IEEE International Instrumentation and Measurement Technology Conference* (Singapore: Suntec Singapore International Convention & Exhibition Centre, 2009).

30. M. Weigert, U. Schmidt, T. Boothe, et al., "Content-Aware Image Restoration: Pushing the Limits of Fluorescence Microscopy," *Nature Methods* 15, no. 12 (2018): 1090–1097.

31. T. Eelbode, J. Bertels, M. Berman, et al., "Optimization for Medical Image Segmentation: Theory and Practice When Evaluating With Dice Score or Jaccard Index," *IEEE Transactions on Medical Imaging* 39, no. 11 (2020): 3679–3690.

32. H. Wang, M. Xian, and A. Vakanski, "Bending Loss Regularized Network for Nuclei Segmentation in Histopathology Images," in *Proceedings – International Symposium on Biomedical Imaging* (IEEE Computer Society, 2020), 258–262.

33. A. Kirillov, K. He, R. Girshick, C. Rother, and P. Dollár, "Panoptic Segmentation," 2018, http://arxiv.org/abs/1801.00868.

34. D. P. Huttenlocher, G. A. Klanderman, and W. J. Rucklidge, "Comparing Images Using the Hausdorff Distance," *Analysis and Machine Intelligence* 15 (1993): 850–863.

35. R. Wang, H. Jiang, and Y. Li, "UPerNet With ConvNeXt for Semantic Segmentation," in *IEEE 3rd International Conference on Electronic Technology, Communication and Information* (Institute of Electrical and Electronics Engineers Inc., ICETCI, 2023), 764–769.

36. B. Zhou, H. Zhao, X. Puig, et al., "Semantic Understanding of Scenes Through the ADE20K Dataset," *International Journal of Computer Vision* 127, no. 3 (2019): 302–321.

37. M. Salvi, A. Mogetta, K. M. Meiburger, et al., "Karpinski Score Under Digital Investigation: A Fully Automated Segmentation Algorithm to Identify Vascular and Stromal Injury of Donors' Kidneys," *Electronics* 9, no. 10 (2020): 1–16.

38. M. Salvi, K. M. Meiburger, and F. Molinari, "Softmax-Driven Active Shape Model for Segmenting Crowded Objects in Digital Pathology Images," *IEEE Access* 12 (2024): 30824–30838.

Supporting Information

Additional supporting information can be found online in the Supporting Information section.